



Hardness recovery mechanism in the heat-affected zone during long-term natural aging and its influence on the mechanical properties and fracture behavior of friction stir welded 2024Al–T351 joints

Z. Zhang, B.L. Xiao, Z.Y. Ma*

Shenyang National Laboratory for Materials Science, Institute of Metal Research, Chinese Academy of Sciences, 72 Wenhua Road, Shenyang 110016, China

Received 13 March 2014; received in revised form 8 April 2014; accepted 9 April 2014
Available online 7 May 2014

Abstract

The microstructural evolution in the heat-affected zone (HAZ) of 5 mm thick friction stir welded (FSW) 2024Al–T351 joints during long-term natural aging and its effect on mechanical properties were investigated by a combination of transmission electron microscopy, atom probe tomography, differential scanning calorimetry and mechanical property tests. FSW thermal cycle resulted in two low hardness zones (LHZs) in the HAZ: LHZ I, near the nugget zone (NZ), with grain coarsening and the dissolution of Guinier–Preston–Bagaryatsky (GPB) zones and solute clusters, as well as the formation and coarsening of S (Al_2CuMg) phases; and LHZ II, far from the NZ, with the dissolution of GPB zones and solute clusters. After 4–12 months of natural aging, the hardness recovered in the LHZ II due to the increase in number densities of Cu–Mg, Cu and Mg clusters, while there was no obvious change in the microstructure and hardness in LHZ I. The tensile strength of FSW 2024Al–T351 joints increased as the welding speed increased from 100 to 400 mm min^{-1} and was weakly enhanced by the long-term natural aging, but was independent of the rotation rates from 400 to 1200 rpm. The FSW joints fractured along LHZ I under a low welding speed of 100 mm min^{-1} . With the increase of the welding speed and the prolongation of natural aging time, the joints fractured at LHZ I, LHZ II or the interface of the NZ/thermo-mechanically affected zone. The variation in the fracture locations was rationalized based on the microstructural evolution.

© 2014 Acta Materialia Inc. Published by Elsevier Ltd. All rights reserved.

Keywords: Aluminum alloys; Friction stir welding; Aging; Mechanical properties; Microstructure

1. Introduction

The 2024 aluminum alloy, as a widely used principal damage-tolerant material in the aerospace industry in wing and fuselage structures [1], is usually fastened together using rivets due to its poor weldability by fusion processes [2]. Driven by the need for low cost and weight saving, developing a suitable joining technology (especially high-quality welding procedures) for this alloy to replace the rivets and

fasteners is of critical importance [3]. Friction stir welding (FSW), a technology characterized by the plastic flow without melting of base material (BM), is a new alternative welding technology for the 2024Al alloy, and meets this need [4].

For precipitation-hardened aluminum alloys (2xxx, 6xxx and 7xxx), the thermo-mechanical process during FSW results in the change in the distribution, size and density of the precipitates in various zones [5–11]. The temperature reached in the nugget zone (NZ) is sufficiently high to induce the dissolution of the hardening precipitates [5–8]. The two sides of the NZ are commonly referred to as

* Corresponding author. Tel./fax: +86 24 83978908.
E-mail address: zyrna@imr.ac.cn (Z.Y. Ma).

the thermo-mechanically affected zone (TMAZ), which experiences lower heat input and smaller plastic deformation. Outside of the TMAZ is the heat affected zone (HAZ), which is subjected only to the thermal cycle. Generally, the HAZ has the low hardness zone (LHZ) due to significant dissolution/coarsening of the precipitates and plays an important role in determining the mechanical properties and fracture behavior of the FSW joints [5–11].

For FSW 2024Al–T351 joints, the microstructure evolution has been characterized in a number of studies. Genevois et al. [6] quantitatively examined the precipitate (Guinier–Preston–Bagaryatsky (GPB) zones and S phase) distribution from the NZ to the BM in the FSW 2024Al–T351 joint under a rotation rate of 800 rpm and a welding speed of 100 mm min⁻¹. Jones et al. [12] investigated the correlation between microstructures and microhardness of the FSW 2024Al–T351 joint under an unspecified welding parameter. It was reported that the heat input induced different degrees of dissolution/coarsening of the precipitates at varied positions, and therefore produced two LHZs on both the advancing side (AS) and the retreating side (RS) of the joint: one is near the NZ and the other is far from the NZ. They inferred that the hardness of the LHZ far from the NZ may recover during long-term post-weld natural aging; however, they did not provide convincing microstructural evidence to support their judgement. Zhang et al. [13] reported that FSW 2024Al–T351 joints may fracture at the NZ, NZ/TMAZ interface or LHZ under different welding speeds. However, the detailed microstructure examination and mechanical property test of FSW 2024Al–T351 joints are absent. Recently, Fu et al. [14] investigated the effect of 1 year post-weld natural aging on the microstructures and microhardness of a 1.6 mm thickness FSW 2024Al–T351 joint. Their results showed that the LHZs were all located in the NZ, which was different from the result of Refs. [5–12].

The precipitation sequence of 2024Al alloy is complicated and remains controversial. The general precipitation sequence from the supersaturated solid solution (SSSS) during artificial aging was originally recognized as [15]: SSSS → GPB zones → S''/GPB2 → S' → S. However, the structure of S'' has not been clearly confirmed. The structure of the S' phase is identical to that of the equilibrium S phase but with varying lattice dimensions; they are therefore considered to be the precursor type of the S phase [16,17]. Recently, the solute clusters, containing several to tens of solute atoms and fully coherent with the matrix, were recognized as important precipitates in 2024Al alloy [18,19]. Their structure is very difficult to resolve, even using high resolution transmission electron microscopy (HRTEM), but could be convincingly identified using atom probe tomography (APT) [18]. Moreover, the GPB zones were thought to be associated with solute clusters and do not reflect accurately the decomposition and hardening processes in Al–Cu–Mg alloys [19,20]. Even though extensive experimental data have been presented in a range of works, the composition and structure of the GPB zones

are still controversial. Hence, the term “GPB zones” is still used to facilitate understanding in this study. The precipitation sequence during artificial aging was therefore revised as: SSSS → solute clusters → solute clusters + GPB zones → solute clusters + GPB zones + S → S [21].

The 2024Al alloy has a strong natural aging tendency. For FSW 2024Al joints, the HAZ is a wide zone and experienced different non-isothermal thermal cycles under varied welding parameters. The dissolved precipitates re-precipitate after welding. The LHZ far from the NZ and the LHZ near the NZ may exhibit different natural aging responses. This will definitely change the mechanical properties of the FSW joints during the time that the welded components are in service. Thus, a systematical investigation of the effect of natural aging on the microstructural evolution in the HAZ of FSW 2024Al–T351 joints under a wide range of FSW parameters is of critical importance to optimize the mechanical behavior of the joints. However, such an investigation is lacking.

In the present work, 5 mm thick 2024Al–T351 plates were friction stir welded under varied welding parameters. Temperature measurement and microstructure (GPB zones, S phase and solute clusters) observation of two LHZs were undertaken. The effect of post-weld natural aging time on the FSW joints was systematically examined. The aim is to understand the effect of natural aging on the microstructures and mechanical properties of FSW 2024Al–T351 joints.

2. Experimental procedure

A 6.5 mm thick commercial Alclad 2024Al–T351 rolled plate was used in this study as the BM. The nominal chemical compositions and the tensile properties of the plate are listed in Table 1. The plates, with a length of 400 mm and a width of 70 mm, were machined on both sides to 5.0 mm thickness to remove the Alclads, and then were butt-welded along the rolling direction with a tool tilt angle of 2.75° using a FSW machine (China FSW Center, Beijing, China). A tool with a concave shoulder 20 mm in diameter and a threaded cylindrical pin 8 mm in diameter and 4.8 mm in length was used. The FSW parameters used in this study are summarized in Table 2.

In order to study the role of post-weld natural aging in service, the FSW samples were naturally aged at room temperature for 24, 96 and 168 h (short-term natural aging, SNA), and 2880 and 8670 h (long-term natural aging, LNA), respectively. The FSW samples were designated in brief forms. For example, sample SNA-800-100-24 (96, 168) h denotes the sample welded at a rotation rate of 800 rpm and a welding speed of 100 mm min⁻¹ with a 24 (96, 168) h short-term natural aging; sample LNA-800-100-2880 (8670) h denotes the sample welded at 800 rpm and 100 mm min⁻¹ with a 2880 (8670) h long-term natural aging.

All the FSW samples were cross-sectioned perpendicular to the welding direction using an electrical discharge

Table 1
Chemical compositions and mechanical properties of 2024Al–T351 rolled plate.

Chemical composition								Mechanical property		
Cu	Mg	Mn	Fe	Si	Zn	Ti	Al	Yield stress (MPa)	Ultimate tensile stress (MPa)	EI (%)
4.43	1.45	0.67	0.16	0.30	0.05	0.03	Bal.	338	480	21

Table 2
Welding parameters of FSW 2024Al–T351 joints.

Sample	Rotation rate R (rpm)	Welding speed V (mm min ⁻¹)	Natural aging time (h)	Designation
1	400	100	168	SNA-400-100-168 h
2	800	100	24, 96, 168	SNA-800-100-24 (96, 168) h
3	1200	100	168	SNA-1200-100-168 h
4	800	200	168	SNA-800-200-168 h
5	800	400	168	SNA-800-400-168 h
6	800	100	2880, 8760	LNA-800-100-2880 (8760) h
7	800	200	2880, 8760	LNA-800-200-2880 (8760) h
8	800	400	2880, 8760	LNA-800-400-2880 (8760) h

machine. The hardness measurement was conducted along the mid-thickness of the transverse cross-section of the welds using an automatic tester (LECO, LM-247AT) under a load of 500 g for 13 s. After two LHZs were identified, the temperature histories at these regions were recorded by embedding the thermocouples in these two LHZs, respectively. The temperature data were sampled at an interval of 0.04 s by a temperature recorder.

Metallographic observation was carried out by optical microscopy (OM, Axiovert 200 MAT). The samples for OM were ground and polished and then etched using Keller's reagent (190 ml water, 2 ml hydrofluoric acid, 3 ml hydrochloric acid and 5 ml nitric acid). The precipitate distributions in as-welded joints were observed by transmission electron microscopy (TEM, TECNAI 20). Thin films for TEM, which were cut from the corresponding locations in the weld using an electrical-discharge machine, were prepared by jet electro-polishing using a solution of 70% methanol and 30% nitric at 243 K (–30 °C) and 19 V. Meanwhile, a differential scanning calorimeter (DSC, Q1000) was used to follow the structure evolution of LHZs with various states during heating at a rate of 10 °C min⁻¹. Much care was taken to ensure location-to-location correspondence between the examinations and hardness measurements.

Small rods of 0.5 × 0.5 × 10 mm for APT were cut from the LHZ far from the NZ of sample 800-100 with different natural aging times, and were then prepared by a standard two-step electro-polishing method [22]. APT analysis was performed on a local electrode atom probe (LEAP) 3000 HR at a temperature of 30 K. All measurements were performed with a pulse fraction of 15% under an ultra-high vacuum condition of $\sim 1 \times 10^{-8}$ Pa. The detector efficiency of this instrument was previously demonstrated to be 57% [23]. The reconstruction procedure and analysis were conducted using the software package IVAS 3.4.3 from Imago Scientific Instruments Corporation (Madison, WI, USA). In order to discern the number of the solute clusters from the reconstructed APT data, the clustering atoms selected

were Cu and Mg and a maximum separation distance, d_{\max} , of 0.7 nm and a minimum number of atoms, N_{\min} , of 2 atoms were employed using the maximum separation algorithm [24]. After obtaining the (Cu, Mg) clusters data, Cu–Mg, Cu and Mg clusters were manually identified, respectively.

In order to obtain the real mechanical properties and fracture locations of the joints, the joint surfaces for the tensile specimens were planed with abrasive papers to ensure the equal cross-sectional area at various locations of the joints. The configuration and size of the transverse tensile specimens are shown in Fig. 1. Room-temperature tensile tests were carried out using the Zwick–Roell testing machine at a strain rate of 4.0×10^{-4} s⁻¹ and the tensile properties of each joint reported were the averages of three test results.

3. Results

3.1. Microhardness map

Fig. 2 shows the microhardness profiles of the FSW 2024Al–T351 joints under various welding parameters and natural aging times. These hardness profiles can be classified into five groups. The effect of the rotation rate on the hardness profiles of the SNA FSW samples at a welding speed of 100 mm min⁻¹ is shown in Fig. 2a. The double “W” shaped hardness profiles exhibited two LHZs on both RS and AS of the joints. The LHZs near and far

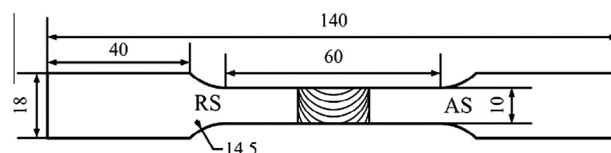


Fig. 1. Configuration and size of tensile specimen.

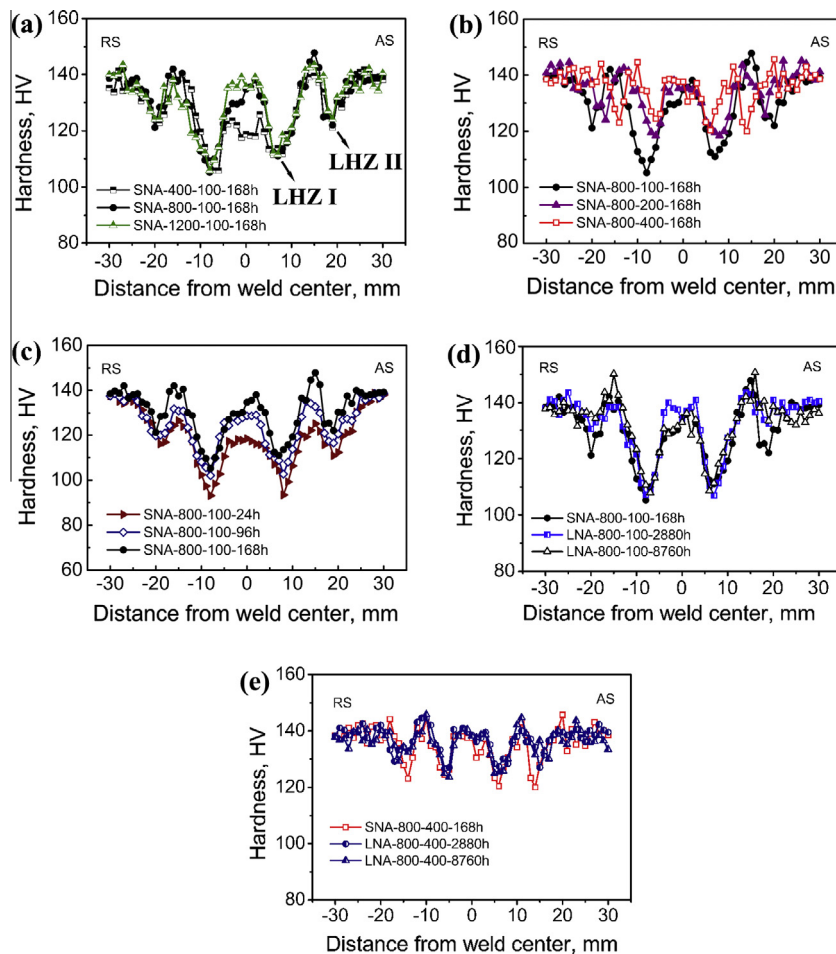


Fig. 2. Hardness profiles of FSW 2024 Al-T351 joints showing effect of (a) rotating rate, (b) welding speed, (c) short-term natural aging time, (d and e) long-term natural aging time.

from the NZ were defined as LHZ I and LHZ II, respectively, in this work (as shown in Fig. 2a). The hardness of the NZ was lower than that of the BM and it reached its minimum in LHZ I and LHZ II, which were ~ 8 mm and 20 mm from the centerline of the joint, respectively. It can be seen that increasing the rotation rate from 400 to 1200 rpm exerted no noticeable influence on the hardness and locations of LHZ I and LHZ II, but increased the hardness of the NZ and made the hardness distribution more uniform. Fig. 2b shows the effect of the welding speed on the hardness profiles of the SNA FSW samples. When increasing the welding speed from 100 to 400 mm min⁻¹, the hardness of LHZ I increased gradually while the hardness of LHZ II was essentially unchanged. Furthermore, it is noted that when increasing the welding speed from 100 to 400 mm min⁻¹, the locations of both LHZ I and LHZ II moved inwards to the centerline of the joint.

Fig. 2c and d shows the effects of short-term and long-term natural aging times, respectively, on the hardness profiles of sample 800-100. It can be seen that the hardness increased in both LHZs I and II after 7 days (168 h) of natural aging (Fig. 2c). However, after 4 months (2880 h) of natural aging, the hardness was unchanged in LHZ I but

increased and approached the BM level in LHZ II. Further increasing the natural aging time to 12 months (8760 h) did not result in an obvious increase in the hardness of LHZ II (Fig. 2d). For sample 800-200, the effect of natural aging time on the hardness profile is similar to that for sample 800-100 and is therefore not shown. For sample 800-400, after 168 h of short-term aging (sample SNA-800-400-168 h), the hardness of LHZ II was slightly lower than that of LHZ I (Fig. 2e). However, when increasing the natural aging time further, the hardness at LHZ II recovered significantly, whereas recovery of the hardness in LHZ I was not distinct. In this case, the hardness of LHZ II was higher than that of LHZ I for samples 800-400 with the long-term natural aging. Another noteworthy finding is that the hardness of the NZ was more homogeneous after the long-term natural aging.

3.2. Microstructure characteristics

Fig. 3 shows the cross-sectional macrostructures of the FSW 2024Al-T351 joints. For all the FSW joints, no welding defect was detected. Three zones, i.e. NZ, TMAZ and HAZ, were discernible. According to the role of shoulder

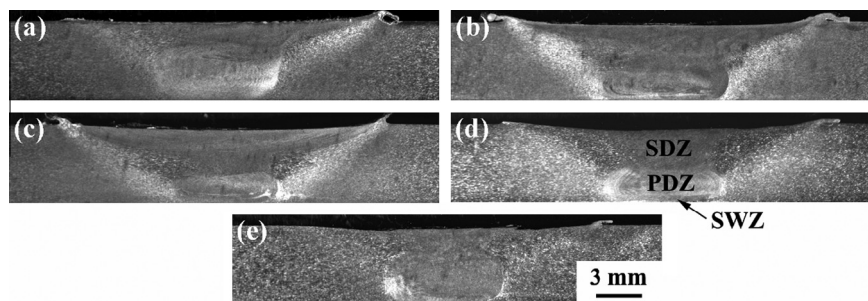


Fig. 3. Cross-sectional macrostructures of FSW 2024Al-T351 joints: (a) 400-100, (b) 800-100, (c) 1200-100, (d) 800-200, (e) 800-400.

and pin in the formation of the NZ, the NZ can be subdivided into three sub-zones: the shoulder-driven zone (SDZ), the pin-driven zone (PDZ) and the swirl zone (SWZ) (marked out in Fig. 3d) [13,25,26]. The most striking feature is that the shapes of the SDZ and PDZ were apparently affected by the rotation rate and welding speed. A comparatively large PDZ with indistinct onion-ring formations and a small SDZ were observed in the NZ of sample 400-100 (Fig. 3a). When increasing the rotation rate from 400 to 800 rpm, the SDZ enlarged and the PDZ shrunk simultaneously (Fig. 3b). This trend was further extended as the rotation rate was further increased to 1200 rpm (Fig. 3c). At a rotation rate of 800 rpm, increasing the welding speed from 100 to 200 mm min⁻¹ resulted in the narrowing of the SDZ but only minor variation of the PDZ. Further increasing the welding speed from 200 to 400 mm min⁻¹, the SDZ went on shrinking and became very small, while at the same time the PDZ enlarged obviously. The changing trend in the shapes of the SDZ and PDZ for the present FSW 2024Al-T351 joints was in agreement with the results reported by Arbegast [26].

Fig. 4 shows the OM micrographs of the BM, NZ, TMAZ, LHZ I and LHZ II of sample 800-200. It can be seen that the elongated grains of the BM resulting from the rolling process were 100–200 μm long and ~10–50 μm wide (Fig. 4a). In the NZ, the fine and equiaxed grain structure with an average grain size of ~12 μm indicated the occurrence of dynamic recrystallization under the severe plastic deformation and thermal exposure (Fig. 4b). The upward elongated grains were observed in the TMAZ (Fig. 4c), which underwent less plastic deformation and lower heat input. Thus there was no recrystallization in this zone. Notably coarsened grains were observed in LHZ I (Fig. 4d), in which the plastic deformation was absent and only heat input played a role. In contrast, the grain microstructure of LHZ II was identical with that of the BM (Fig. 4e).

Fig. 5 shows the bright-field TEM images and associated diffraction patterns of the BM, LHZ I and LHZ II of sample SNA-800-100-168 h. Rod shaped phases and dislocations were observed in the BM (Fig. 5a and b). The GPB zones of the BM were indiscernible under conventional TEM, but could be detected by diffuse streaks in the diffraction pattern (insert in Fig. 5b). The incoherent rod

shaped phases with a typical size of 50–100 nm across and up to 500 nm in length were Ω (Al₂₀Cu₂Mn₃) phases [27,28]. The microstructure of LHZ I was characterized by a high density of needle-shaped S (Al₂CuMg) precipitates and few Ω phases (Fig. 5c). In contrast, the microstructure of LHZ II was similar to the BM, but the diffraction pattern showed that there were no GPB zones in this zone (Fig. 5d).

Fig. 6 shows the bright-field TEM images and associated diffraction patterns of LHZ I and LHZ II of samples LNA-800-100-2880 h and LNA-800-400-2880 h. The microstructures in LHZ I and LHZ II of sample LNA-800-100-2880 h, as shown in Fig. 6a and b, were basically identical with those of sample SNA-800-100-168 h. The diffraction pattern showed that there were no GPB zones in LHZ II (Fig. 6b), indicating that the GPB zones did not form in LHZ II during the long-term post-weld natural aging. For sample LNA-800-400-2880 h, the density of the S precipitates significantly decreased in LHZ I compared with that for sample LNA-800-100-2880 h, while there was no obvious change in the precipitates in LHZ II (Fig. 6c and d).

3.3. Atom probe tomography

Fig. 7a–c shows the typical three-dimensional (3-D) reconstruction of the raw experimental data, solute clusters and enlarged 3-D map of individual clusters, respectively, for LHZ II of sample SNA-800-100-168 h. It can be seen that the solute clusters are evenly distributed. Similarly, the solute clusters for LHZ II of sample LNA-800-100-2880 h also exhibit a uniform distribution.

In fact, it is not possible to discern any obvious pattern in the solute distribution by simple visual inspection. In order to facilitate the comparison, the number densities of the Cu–Mg, Cu and Mg clusters vs. the cluster size of 2–15 atoms for both samples are provided in Fig. 8a–c, respectively. All the number densities of the Cu–Mg, Cu and Mg clusters in sample LNA-800-100-2880 h increased compared to those in sample SNA-800-100-168 h (Fig. 8a–c). The detailed number densities of the three cluster types (Cu–Mg, Cu and Mg) for LHZ II of samples SNA-800-100-168 h and LNA-800-100-2880 h are listed in Table 3. Table 3 indicates that the Cu–Mg clusters had

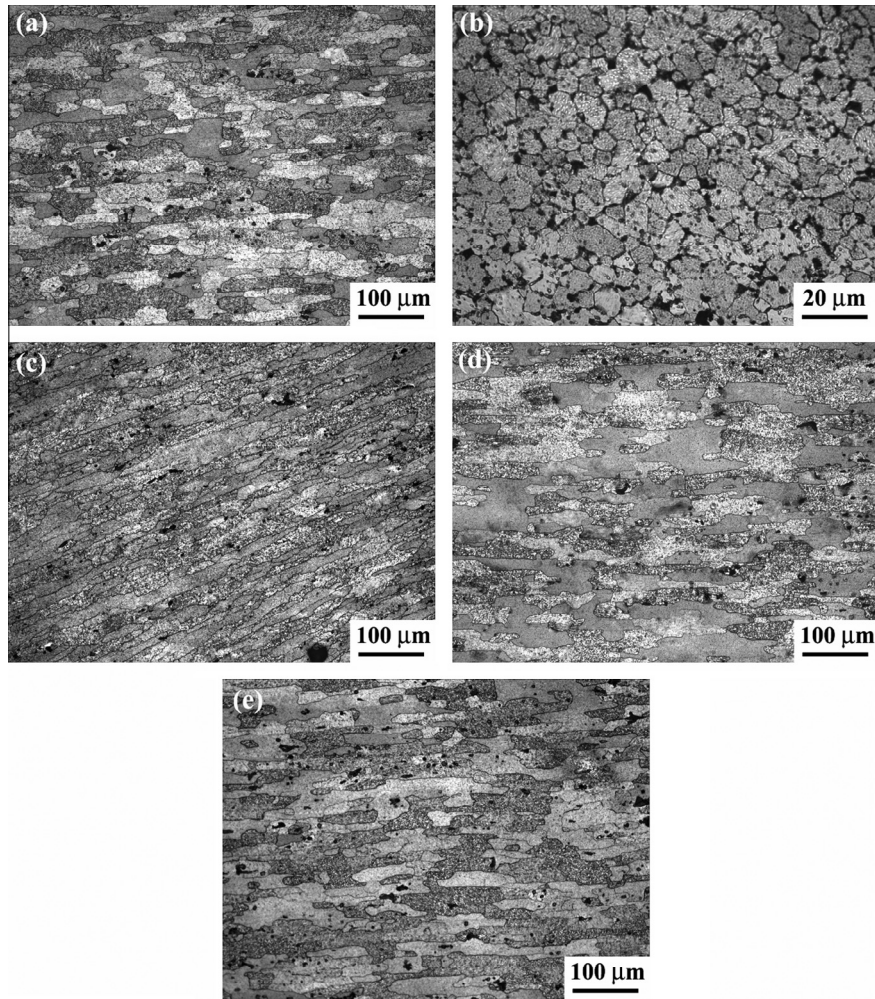


Fig. 4. Optical micrographs of sample 800-200: (a) BM, (b) NZ, (c) TMAZ, (d) LHZ I and (e) LHZ II.

the largest number density and possessed almost half of the total amount of solute clusters per cm^3 . It should be pointed out that there is no significant change in the Mg/Cu ratio of Cu–Mg clusters for these samples.

It should be noted that experimental observations using APT are strongly influenced by the limited detection efficiency of the APT instrument ($\sim 50\%$) and by the statistical analysis of the data [29]. However, these effects are equal for each sample investigated, and a comparison of number density is therefore appropriate.

3.4. DSC curves

Fig. 9a and b shows the DSC curves of LHZs I and II of samples 800-100 under the natural aging times of 24 h, 168 h, 2880 h and 8760 h, respectively. For comparison, the DSC curve of the BM is given in two plots. Three effects were observed in this study. Exothermic peak A, between 60 and 150 °C with a peak at ~ 110 °C, is due to the formation of solute clusters (mainly Cu–Mg clusters) [19,20], which become unstable at higher temperatures. Endothermic peak B, between 150 and 240 °C with a peak

at ~ 230 °C, is thought to be due to the dissolution of these solute clusters [19]. For the BM, the dissolution of GPB zones (GPB zones were detected by TEM, see Section 3.2) will also contribute to the endothermic peak B [27]. The presence of the dissolution effect for all samples shows that all samples contain the solute clusters. Exothermic peak C, between ~ 230 and 340 °C, is attributed to the formation of S phases [30,31]. This study is mainly concerned with peaks A and B, and the following findings are made.

For LHZ I (Fig. 9a), no peak A was observed, and peaks B and C were lower than those for the BM. For peak B, there was a sharp increase in the peak intensity when increasing the natural aging time from 24 to 168 h. However, further increasing the natural aging time from 168 to 2880 h resulted in only a very tiny increase in the intensity of peak B, and no change of peak B occurred with further increasing the natural aging time from 2880 to 8760 h. This indicates that the solute clusters formed mainly during the early stage of natural aging (less than 168 h).

For LHZ II (Fig. 9b), peak A was observed in sample 800-100-24 h. When increasing the natural aging time from 24 to 168 h, peak A disappeared. Further increasing the

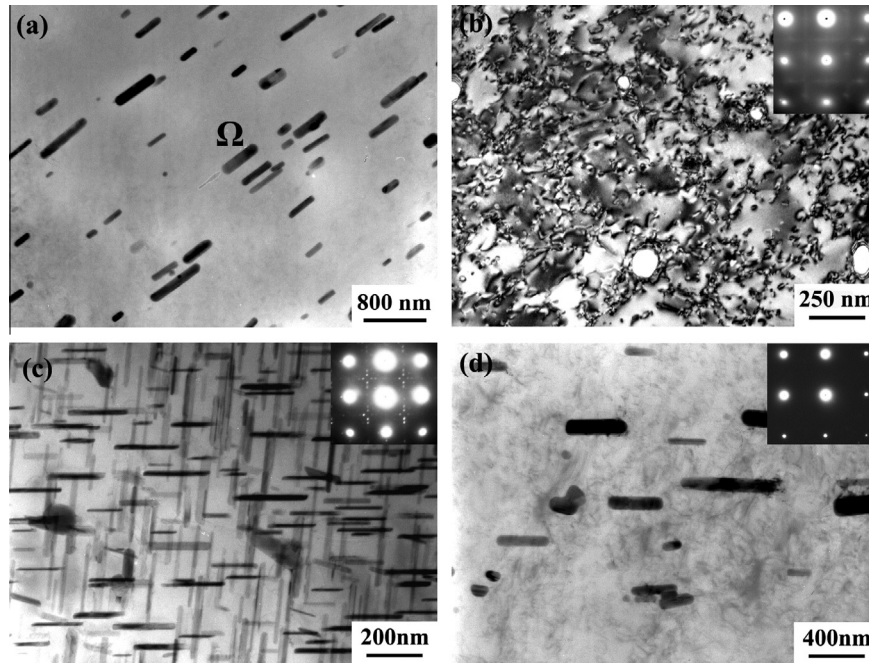


Fig. 5. Bright-field TEM micrographs and associated diffraction patterns of sample SNA-800-100-168 h with a [100] zone axis: (a) and (b) BM, (c) LHZ I and (d) LHZ II.

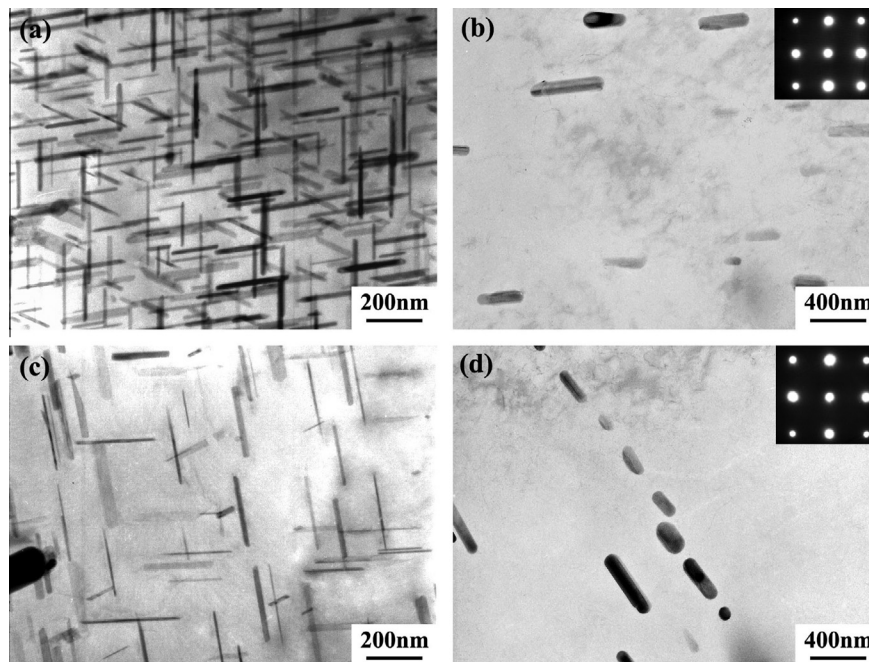


Fig. 6. Bright-field TEM micrographs and associated diffraction patterns with a [001] zone axis: (a) LHZ I and (b) LHZ II of sample LNA-800-100-2880 h; (c) LHZ I and (d) LHZ II of sample LNA-800-400-2880 h.

natural aging time from 168 to 2880 h, peak B exhibited a large increase. As the natural aging time increased further from 2880 to 8760 h, peak B for LHZ II slightly increased and was still lower than that for the BM. This indicates that in LHZ II, the GPB zones and solute clusters dissolved during FSW and substantial solute clusters formed during the long-term natural aging (more than 4 months).

3.5. Temperature distribution

The temperature histories during FSW recorded in LHZs I and II of samples 800-100 and 800-400 are shown in Fig. 10. Profiles A and B correspond to the thermal cycles of LHZ II for samples 800-400 and 800-100, respectively. Profiles C and D correspond to the thermal cycles of

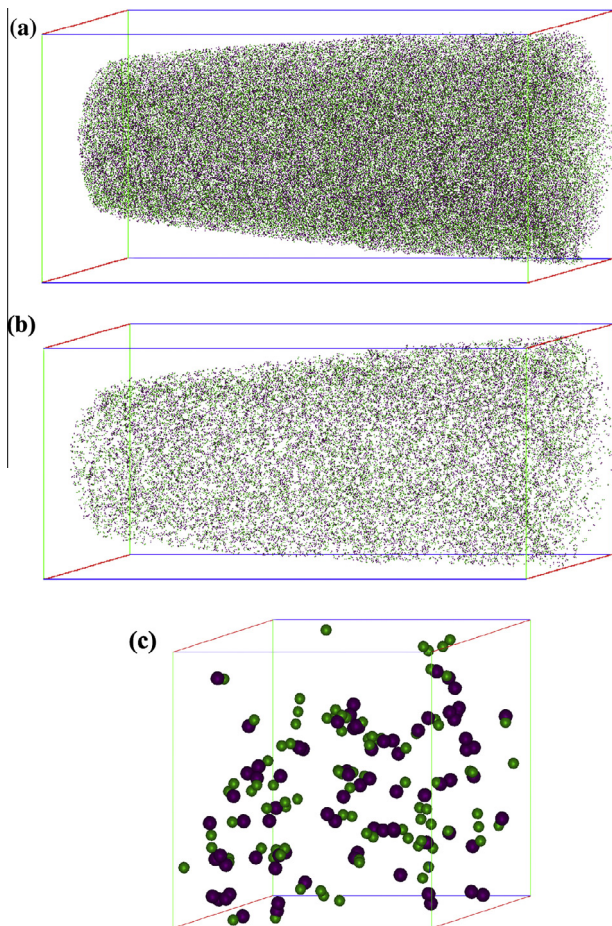


Fig. 7. 3-D APT maps of sample SNA-800-100-168 h: (a) raw data of Cu and Mg atoms (green = Cu, purple = Mg), (b) clusters data (these maps have a dimension of $50 \times 50 \times 130$ nm), (c) enlarged 3-D map (dimension: $10 \times 10 \times 10$ nm) of individual clusters in (b). (For interpretation of the references to color in this figure legend, the reader is referred to the web version of this paper.)

LHZ I for samples 800-400 and 800-100, respectively. It can be seen that LHZ I experienced approximately the same peak temperatures of 340°C , while LHZ II experienced similar peak temperatures of $200\text{--}220^\circ\text{C}$ for both samples. However, it is noted that sample 800-100 experienced a longer length of thermal exposure than sample 800-400 at higher temperature ranges of above 235°C and 120°C , respectively, for LHZ I and LHZ II.

3.6. Tensile properties and fracture location

In order to accurately locate the tensile fracture location of the joints, the cross-sections of failed specimens were etched. Under the investigated parameters, the joints fractured at three different locations: LHZ I, LHZ II and the NZ/TMAZ interface, respectively, as shown in Fig. 11a–c. Because of disagreement with the LHZs, the unusual fracture location at the NZ/TMAZ interface should be of particular concern and the magnified micrograph of the NZ/TMAZ interface (marked with a white box in Fig. 11c) is shown in Fig. 12a. It shows that the joint

fractured along the SDZ/TMAZ interface at the top and across the onion rings at the bottom. The further magnified micrographs of regions B and C in Fig. 12a show that the fracture path was along some linear microstructures at the SDZ/TMAZ interface while no special feature was observed at the PDZ (Fig. 12b and c).

The statistical distribution of the fracture locations for various FSW samples is presented in Table 4. For samples SNA-400-100-168 h, SNA-800-100-168 h, SNA-1200-100-168 h and LNA-800-100-2880 h under a low welding speed of 100 mm min^{-1} , they fractured in LHZ I. The shear fracture path was a $\sim 45^\circ$ angle to the tensile axis, as shown in Fig. 11a. When increasing the welding speed from 100 to 200 mm min^{-1} , sample SNA-800-200-168 h fractured at the NZ/TMAZ interface on the RS (Fig. 11c), while sample LNA-800-200-2880 h fractured at either LHZ I or the NZ/TMAZ interface. As the welding speed further increased to 400 mm min^{-1} , the fracture location was at either LHZ II (Fig. 11b) or the NZ/TMAZ interface for sample SNA-800-400-168 h, but at either LHZ I or the NZ/TMAZ interface for sample LNA-800-400-2880 h.

The tensile strength of the FSW 2024Al–T351 joints is shown in Table 5. It should be pointed out that although the three tensile specimens might fracture at different locations for both samples 800-200 and 800-400, only small errors existed among the three strength results of the joints, indicating that the change of the fracture locations did not influence the tensile properties of the joints. Table 5 reveals four important findings. Firstly, under a constant welding speed of 100 mm min^{-1} , increasing the rotation rate from 400 to 1200 rpm did not improve the tensile strength of the joints. Secondly, under a constant rotation rate of 800 rpm, the tensile strength increased when increasing the welding speed from 100 to 400 mm min^{-1} . Thirdly, the SNA FSW samples exhibited a larger elongation than the LNA FSW samples. Fourthly, long-term post-weld natural aging slightly increased the tensile strength of samples 800-100, 800-200 and 800-400.

4. Discussion

4.1. Microstructure evolution and hardness recovery mechanism of joints

The main strengthening precipitates of the 2024Al–T351 alloy were conventionally thought to be the GPB zones [6]. Recently, Starink et al. [19] found that the Cu–Mg clusters are the dominating factor for room temperature age hardening of Al–1.2Cu–1.2Mg–0.2Mn and Al–1.9Cu–1.6Mg–0.2Mn alloys. The GPB zones and solute clusters represent the main strengthening component in 2024Al alloy [21]. Thus, both GPB zones and solute clusters should be regarded as the main strengthening precipitates in this study.

Based on the correlation of the precipitate evolution and the hardness distribution, four sub-zones can be named on the transverse cross-section of the FSW 2024Al–T351

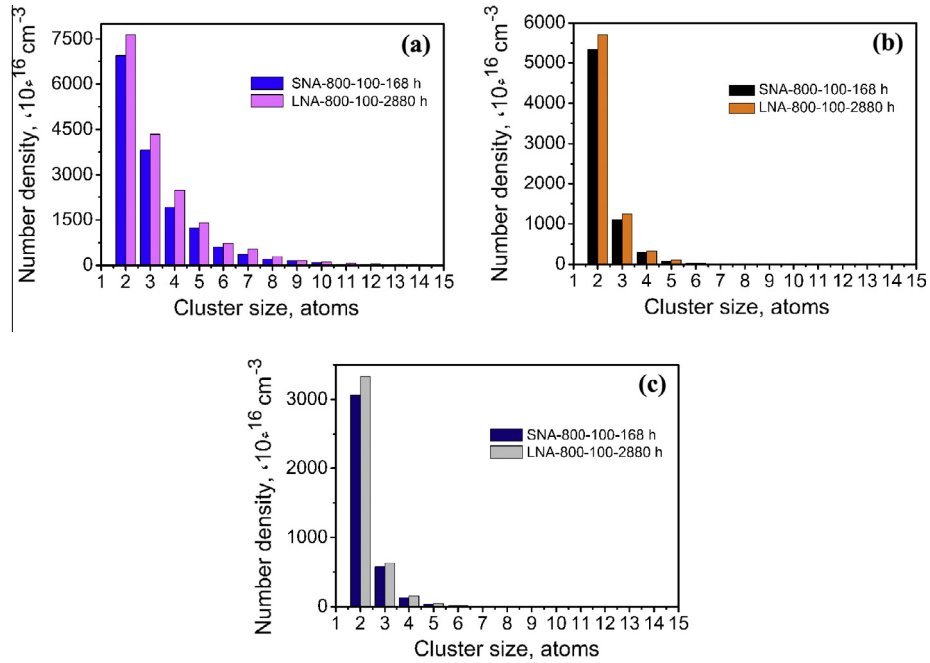


Fig. 8. The number densities vs. cluster size (in atoms) of samples SNA-800-100-168 h and LNA-800-100-2880 h: (a) Cu–Mg clusters, (b) Cu clusters and (c) Mg clusters.

Table 3
Number densities of Cu–Mg, Cu and Mg clusters in LHZ II of samples SNA-800-100-168h and SNA-800-100-2880h (10^{16} cm^{-3}).

Size (atoms)	SNA-800-100-168-h			LNA-800-100-2880 h		
	Cu–Mg	Cu	Mg	Cu–Mg	Cu	Mg
2	6955	5349	3063	7637	5696	3336
3–5	6966	1484	618	8210	1682	828
6–10	2108	37	20	2923	50	21
11–50	191	0	0	293	0	0

joints, as shown in Fig. 13, i.e. the redissolution zone, over-aging zone, peak aging zone and reversion zone, which correspond to the NZ, LHZ I, the region between LHZ I and LHZ II, and LHZ II, respectively.

The GPB zones and solute clusters dissolved under the high temperature and large plastic deformation in the NZ, which was named the redissolution zone. In this zone, the GPB zones re-formed after 4–7 days of natural aging [6,12], which may also coincide with the formation of solute clusters. A higher rotation rate led to a higher temperature and then a higher level of dissolution of the GPB zones and solute clusters, implying that more GPB zones and solute clusters could re-form during the subsequent natural aging. This accounts for higher and more uniform hardness of the NZ in high rotation rate joints (Fig. 2a). The center of the NZ suffered the highest heat input and could achieve a hardness that is identical to that of the BM for some high rotation rate joints (Fig. 2).

For the peak aging zone, Jones et al. [12] suggested that the maximum hardness was due to the presence of a very fine S phase. It can be inferred that the thermal cycle in this zone was the most suitable for the formation of the fine S

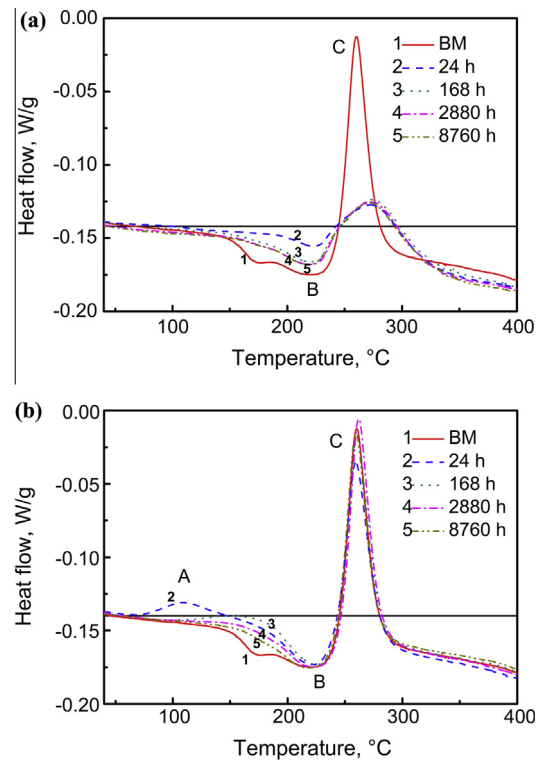


Fig. 9. DSC curves of (a) LHZ I and (b) LHZ II of sample 800-100.

phases and therefore the hardness could reach the maximum (Fig. 2).

Since the mechanical properties of the FSW 2024Al–T351 joints are mainly dependent on the microstructure of the LHZs, the main concern is focused on LHZ I and LHZ II.

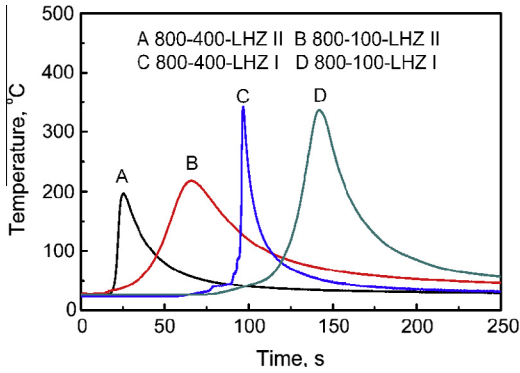


Fig. 10. Temperature histories recorded at LHZs I and II of samples 800-100 and 800-400.

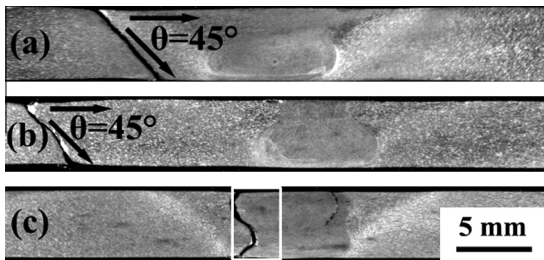


Fig. 11. Typical fracture locations of FSW 2024Al–T351 joints: (a) LHZ I, (b) LHZ II and (c) interface of NZ/TMAZ.

4.1.1. Microstructure evolution and hardness recovery mechanism in LHZ I

For the present FSW 2024Al–T351 joints, LHZ I, i.e. the overaging zone, experienced a fast thermal cycle with a peak temperature of 340 °C (Fig. 10). Based on the

precipitation sequence of 2024Al alloy in Ref. [21], the partial dissolution of the GPB zones and solute clusters in the temperature range of 120–235 °C as well as their partial transformation into the S phase in the temperature range of 235–340 °C occurred. In this case, there are two strengthening origins in LHZ I: the S phase and the solute atoms. The thermal cycle with a peak temperature of 340 °C could create some vacancies in this zone, and the solute clusters re-formed during 7 days of natural aging (168 h) (Fig. 9a). Thus, the hardness of LHZ I increased after 7 days of natural aging for sample 800-100 (Fig. 2c). When further increasing the natural aging time from 168 to 2880 h, only a small number of solute clusters formed (Fig. 9a). This was not reflected on the hardness of LHZ I (Fig. 2d and e) but enhanced the tensile properties of FSW 2024Al–T351 joints (Table 5).

The overaging degree of precipitation-hardened aluminum alloys is related to the welding parameters. The effect of welding speed and rotation rate on the overaging zones of FSW 6061Al–T651 joints have been systematically investigated by Liu and Ma [7]. It was reported that the duration above the phase-transition temperatures shortened as the welding speed increased, similar to the present observation (Fig. 10), but it is independent of the rotation rate. This indicated more severe overaging in LHZ I of sample 800-100 than that of sample 800-400. Thus both hardness and tensile strength of the FSW 2024Al–T351 joints increased with increasing the welding speed from 100 to 400 mm min⁻¹ but were independent of the rotation rate (Table 5). It is noted that the increase of welding speed also resulted in a decrease of heat input. Thus, the locations of the LHZs moved inwards (Fig. 2b). This is consistent with the observation in FSW 6061Al–T651 joints [7].

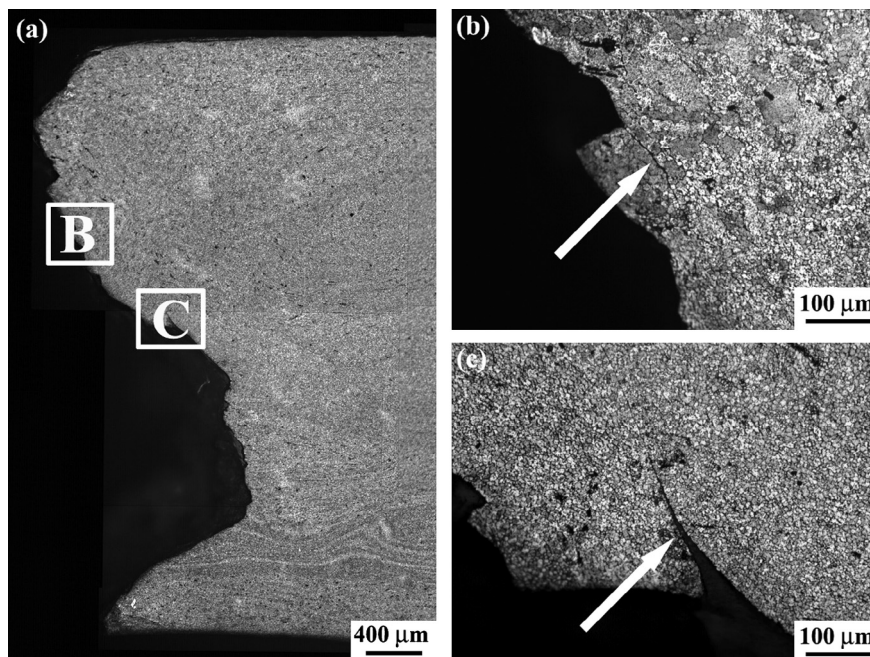


Fig. 12. (a) Magnified micrographs of the marked zone in Fig. 11c; (b and c) further magnified micrographs of regions B and C in Fig. 12a.

Table 4
Statistical distribution of fracture locations of FSW 2024Al–T351 joints.

Sample	Fracture location (three tensile specimens per joint)		
	LHZ I	LHZ II	NZ/TMAZ
SNA-400-100-168 h	3	0	0
SNA-800-100-168 h	3	0	0
SNA-1200-100-168 h	3	0	0
SNA-800-200-168 h	0	0	3
SNA-800-400-168 h	0	2	1
LNA-800-100-2880 h	3	0	0
LNA-800-200-2880 h	2	0	1
LNA-800-400-2880 h	2	0	1

Table 5
Transverse tensile properties of FSW 2024Al–T351 joints.

Sample	El (%)	Ultimate tensile stress (UTS) (MPa)	UTS _{FSW} /UTS _{BM}
SNA-400-100-168 h	7.4	412 ± 0.5	86
SNA-800-100-168 h	7.0	408 ± 0.8	85
SNA-1200-100-168 h	7.8	416 ± 0.2	87
SNA-800-200-168 h	8.0	439 ± 2.0	89
SNA-800-400-168 h	14.7	451 ± 1.3	94
LNA-800-100-2880 h	5.5	420 ± 2.7	88
LNA-800-200-2880 h	6.0	445 ± 2.1	93
LNA-800-400-2880 h	9.0	457 ± 1.5	95

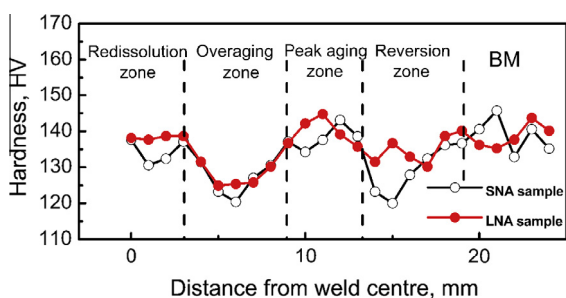


Fig. 13. Schematic diagram showing four sub-zones on transverse cross-section of FSW 2024Al–T351 joints (sample 800-400).

4.1.2. Microstructure evolution and hardness recovery mechanism in LHZ II

For the reversion zone (LHZ II) of the FSW 2024Al–T351 joints, it experienced the welding thermal cycle with the peak temperature of 200–220 °C (Fig. 10), which is equivalent to retrogression and reaging (RRA). During this process, the dissolution of GPB zones (Figs. 5d and 9b) and the decomposition of solute clusters (Fig. 9b) simultaneously occurred. As a result, LHZ II was characterized by a drastic drop in hardness (Fig. 2a and b). As reported in Refs. [32,33], the GPB zones could dissolve in less than 10 s above the phase transition temperature. The dissolution time of the GPB zones for samples 800-100 and 800-400 when increasing the temperature from 120 °C to the peak temperature followed by cooling to 120 °C are 50 and 15.5 s (Fig. 10), respectively. Hence, the welding speeds from 100 to 400 mm min⁻¹ provided sufficient dissolution

times for the GPB zones in LHZ II. That is to say, for all the FSW samples in this study, the GPB zones completely dissolved and therefore they had the identical microstructures in LHZ II. Thus, the hardness of LHZ II of the FSW samples was fundamentally independent of the welding parameters (Fig. 2a and b).

For the slow recovery of hardness in LHZ II of FSW 2024Al–T351 joints, the most widely accepted explanation is that a large number of vacancies were eliminated during the thermal cycle; thus the formation of the GPB zones during the post-weld natural aging was strongly slowed down [6,12]. The recent investigations showed that there was a good corresponding relationship between the hardness and the density, sizes and types of solute clusters for Al–Cu–Mg alloys [18,19,21]. Starink et al. [19] investigated the microstructure of room temperature aged Al–1.2Cu–1.2Mg–0.2Mn and Al–1.9Cu–1.6Mg–0.2Mn alloys and found that the density of clusters increased and the Cu/Mg ratio in the clusters approached unity and the formation of Cu–Mg clusters coincided with the rapid hardness increase during natural aging. Marceau et al. [34] investigated the evolution of solute clusters in an Al–2.5Cu–1.5Mg alloy during secondary aging and found that the secondary rapid hardening response (65 °C) is due to a significant increase in the number density of Cu–Mg clusters.

For LHZ II in this study, the slow recovery of hardness (Fig. 2d and e) correlated with the increase in the densities of Cu–Mg, Cu and Mg clusters (Figs. 8, 9b and Table 3), while no GPB zones or S phase were discerned in this zone (Fig. 6b and d). During this process, there is no significant change in the Mg/Cu ratio of Cu–Mg clusters. This indicates that the solute clusters were the exclusive strengthening phases and the increase in the number densities of Cu–Mg, Cu and Mg clusters is the dominating factor for room temperature age hardening of LHZ II. It should be noted that the experimental results are related to the analysis parameter. For instance, if taking the $N_{\min} = 6$ as in Ref. [19], the solute clusters are nearly exclusive Cu–Mg clusters (atoms ≥ 6 , see Fig. 8a–c and Table 3).

The mechanism of cluster formation is due to vacancy-assisted solute diffusion. It can be inferred that no sufficient vacancies were produced during the non-isothermal thermal cycle with the peak temperatures of 200–220 °C in LHZ II. Hence, the hardness of LHZ II slowly recovered during the long-term natural aging (more than 4 months) (Fig. 2d and e).

4.2. The fracture behavior of the FSW 2024Al–T351 joints

The fracture location of the FSW joints was mainly dependent on the lowest hardness distribution. As mentioned above, the hardness of LHZ I increased when increasing the welding speed, while the hardness of LHZ II was only natural aging time dependent. In this case, for the samples with similar hardness values in LHZ I and LHZ II, it is possible for the lowest hardness distribution

zone to be located in LHZ I or LHZ II after natural aging for different lengths of time, due to the aging strengthening in LHZ II. For example, the lowest hardness distribution zone was located in LHZ II for sample SNA-800-400-168 h, but in LHZ I for sample LNA-800-400-2880 h. Thus it is reasonable for sample SNA-800-400-168 h to fracture in LHZ II and sample LNA-800-400-2880 h to fracture in LHZ I (Table 4).

However, some joints with relatively low heat input fractured at the NZ/TMAZ interface, which could not be explained by the hardness distribution. The linear microstructures at the SDZ/TMAZ interface (Fig. 12c) was identified as linear segregation bands consisting of second-phase particles [12]. The linear microstructures weakened the mechanical properties of the local regions (NZ and SDZ/TMAZ interface). Therefore the NZ/TMAZ interface may be the weakest zone or have an identical tensile strength to the lowest hardness distribution zone (LHZ I or II). Thus, both the LHZs and linear microstructures should be taken into consideration in discussing unusual fracture location.

Focusing on sample 800-200 first, with the hardness of LHZ I less than that of LHZ II (Fig. 2b), the bonding strength of the NZ/TMAZ interface may be slightly less than that of LHZ I in sample SNA-800-200-168 h, but may be identical to that of LHZ I in sample LNA-800-200-2880 h due to the homogeneous hardness recovery of the NZ after the long-term natural aging, which could explain the difference in the fracture locations of samples SNA-800-200-168 h and LNA-800-200-2880 h (Table 4). As for sample 800-400, the lowest hardness distribution zone was located in either LHZ I or LHZ II depending on the natural aging time. Coupled with more uniform hardness distribution of the NZ after the long-term natural aging, the weakest zone may therefore transfer from LHZ II and the NZ/TMAZ interface in sample SNA-800-400-168 h to LHZ I and the NZ/TMAZ interface in sample LNA-800-400. Accordingly, sample 800-400 naturally aged for different lengths of time fractured at varied positions (Table 4).

Based on the results of this study, two considerations need to be emphasized for the applications of FSW 2024Al–T351 joints. Firstly, a long-term natural aging of more than 4 months is necessary to recover the hardness of LHZ II and stabilize the mechanical properties of the joints. Secondly, since the linear microstructures in the NZ resulted in unusual fracture of the joints along the NZ/TMAZ interface, their effect on the fatigue properties of the joints deserves further evaluation.

5. Conclusions

- (1) Two LHZs (LHZs I and II near and far from the NZ), with different microstructural evolution mechanisms, were observed at both RS and AS of FSW 2024Al–T351 joints. The hardness of LHZ I

increased with increasing the welding speed but was independent of the rotation rate. The hardness of LHZ II was independent of both the welding speed and rotation rate.

- (2) LHZ I experienced an overaging process with the dissolution of GPB zones and solute clusters, as well as the formation and coarsening of S phases, and it would slightly recover during the short-term post-weld natural aging of 168 h and then had the stable hardness during the long-term natural aging. RRA occurred in LHZ II with the dissolution of the GPB zone and the decomposition of solute clusters, and a slow recovery of hardness occurred due to the increase in the number densities of Cu–Mg, Cu and Mg clusters during the long-term post-weld natural aging.
- (3) The tensile strength of the FSW joints increased with increasing the welding speed and could also be slightly enhanced by the long-term post-weld natural aging, but was independent of the rotation rate.
- (4) The fracture behavior of FSW 2024Al–T351 joints was dependent on both the welding speed and long-term natural aging, but not the rotation rate. When increasing the welding speed, the fracture locations of the joints transferred from LHZ I to the NZ/TMAZ interface or LHZ II. The long-term natural aging helped the reversion of LHZ II and therefore tended to transfer the fracture location of the joints to LHZ I.
- (5) The unusual fracture location at the NZ/TMAZ interface was related with the linear microstructures at the SDZ of the NZ.

Acknowledgement

This work was supported by the National Natural Science Foundation of China under Grant No. 51331008.

References

- [1] Lefebvre F, Ganguly S, Sinclair I. *Mater Sci Eng A* 2005;397:338.
- [2] Fersini D, Pironi A. *Eng Fract Mech* 2007;74:468.
- [3] Jeong DY, Orringer O, Sih GC. *Theor Appl Fract Mech* 1995;22:127.
- [4] Sutton MA, Yang B, Reynolds AP, Taylor R. *Mater Sci Eng A* 2002;323:160.
- [5] Sato YS, Kokawa H. *Metall Mater Trans A* 2001;32:3023.
- [6] Genevois C, Deschamps A, Denquin A, Doisneau-cottignies B. *Acta Mater* 2005;53:2447.
- [7] Liu HJ, Fujii H, Maeda M, Nogi K. *J Mater Process Technol* 2003;142:692.
- [8] Liu FC, Ma ZY. *Metall Mater Trans A* 2008;39:2378.
- [9] Ren SR, Ma ZY, Chen LQ. *Scr Mater* 2007;56:69.
- [10] Aydin H, Bayram A, Uguz A, Akay KS. *Mater Des* 2009;30:2211.
- [11] Aydin H, Bayram A, Uguz A, Durgun I. *Mater Des* 2010;31:2568.
- [12] Jones MJ, Heurtier P, Desrayaud C, Montheillet F, Allehaux D, Driver JH. *Scr Mater* 2005;52:693.
- [13] Zhang Z, Xiao BL, Ma ZY. *Metall Mater Trans A* 2013;44:4081.
- [14] Fu RD, Zhang JF, Li YJ, Kang J, Liu HJ, Zhang FC. *Mater Sci Eng A* 2013;559:319.
- [15] Bagaryatsky YA. *Dokl Akad SSSR* 1952;87:397.

- [16] Wang SC, Starink MJ. *Int Mater Rev* 2005;50:193.
- [17] Winkelman GB, Raviprasad K, Muddle BC. *Acta Mater* 2007;55:3213.
- [18] Marceau RKW, Sha G, Ferragut R, Dupasquier A, Ringer SP. *Acta Mater* 2010;58:4923.
- [19] Starink MJ, Gao N, Davin L, Yan J, Cerezo A. *Philos Mag* 2005;85:1395.
- [20] Starink MJ, Wang SC. *Acta Mater* 2009;57:2376.
- [21] Sha G, Marceau RKW, Gao X, Muddle BC, Ringer SP. *Acta Mater* 2011;59:1659.
- [22] Miller MK, Cerezo A, Hetherington MG, Smith GDW. *Atom probe field ion microscopy*. Oxford: Oxford University Press; 1996.
- [23] Gault B, Moody MP, De Geuser F, Tsafnat G, La Fontaine A, Stephenson LT, et al. *J Appl Phys* 2009;105:034913.
- [24] Miller MK. *Atom probe tomography*. New York: Kluwer Academic/Plenum; 2000.
- [25] Kumar K, Kailas SV. *Mater Sci Eng A* 2008;485:367.
- [26] Arbegast WJ. *Scr Mater* 2008;58:372.
- [27] Wang SC, Lefebvre F, Yan JL, Sinclair I, Starink MJ. *Mater Sci Eng A* 2006;431:123.
- [28] Cheng S, Zhao YH, Zhu YT, Ma E. *Acta Mater* 2007;55:5822.
- [29] Starink MJ, Cao LF, Rometsch PA. *Acta Mater* 2011;60:4194.
- [30] Starink MJ. *Int Mater Rev* 2004;49:191.
- [31] Char A, Walther T, Alfonso C, Zahra AM, Zahra CY. *Acta Mater* 2000;48:2751.
- [32] Fuller CB, Mahoney MW, Calabrese M, Micono L. *Mater Sci Eng A* 2010;527:2233.
- [33] Shercliff HR, Russel MJ, Taylor A, Dickerson TL. *Mec Ind* 2005;6:25.
- [34] Marceau RKW, Sha G, Lumley RN, Ringer SP. *Acta Mater* 2010;58:1795.